

Vortex-based Interactional Aerodynamic
Analysis and Gradient-based Optimization
Applied to Emerging Technologies

Judd Mehr

A dissertation submitted to the faculty of
Brigham Young University
in partial fulfillment of the requirements for the degree of
Doctor of Philosophy

Andrew Ning, Chair
Steven E. Gorrell
R. Daniel Maynes
Timothy W. McLain

Department of Mechanical Engineering
Brigham Young University

Copyright © 2025 Judd Mehr

All Rights Reserved

Additional Discipline Models for Multi-disciplinary Optimization

Chapter 1

“Is the model true?”. If “truth” is to be the “whole truth” the answer must be “No”. The only question of interest is “Is the model illuminating and useful?”.

— George E. P. Box

In addition to the ducted rotor aerodynamic models introduced in ????, some of the studies in this work required the addition of models for other disciplines as well as some extensions to pieces of the aerodynamic models. Specifically, we will cover the details of the blade section aerodynamic model used in the multi-disciplinary optimization studies in this work, the rotor blade structural model, and the ducted rotor acoustics model. Combined with the previously introduced aerodynamic model, the contents of this chapter will enable the aero-structural-acoustic optimizations of Chapter 2.

1.1 Blade Section Aerodynamic Model

When we start putting multiple disciplines together, we occasionally need to approach one or more of those disciplines differently than we do when making assumptions reasonable for that discipline in isolation. In our case, when we want to address the structures and aerodynamics of a rotor blade together, we need to consider blade section thickness in more detail. Instead of assuming a constant airfoil or constant distribution of airfoils across the blade, we need to allow at least the thickness of the airfoil to change during the optimization. With constant airfoil sections, we can pre-compute the section aerodynamics which simply scale with chord length. As soon as we allow shape changes other than simple uniform scaling, however, we either need to include an airfoil analysis method directly into the optimization routine, or we need to augment our pre-computation approach into a more substantial surrogate model.

A nominal analysis for airfoils of varying thickness is simple enough. In fact, ?? covers nearly all of the theory behind such a model. We note, however, that the most important airfoil thickness effects are mostly viscous in nature, namely: an increase in drag as thickness increases. Therefore we require a method with more tightly coupled inviscid and viscous effects than presented in ??.

In addition, most of the multi-disciplinary optimizations in this work will have designs where the solidity of the ducted rotors is relatively

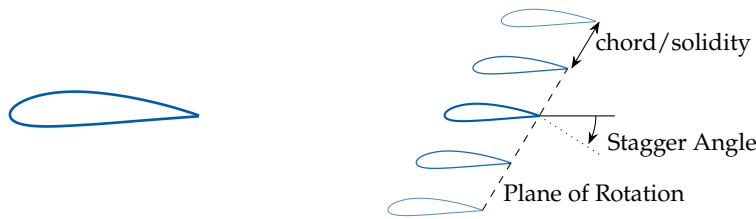


Figure 1.1: An isolated airfoil (left) differs from a linear cascade of airfoils (right) in that the airfoils in the cascade are influenced by the airfoils coming before and after (with decreasing influence out to infinity). The spacing between airfoils is determined by the blade section local solidity, and the skew of the cascade is determined by the stagger angle of the blade section.

high. After a sufficiently high solidity is reached (greater than 0.3), we can no longer consider each blade element as an isolated airfoil, but must treat it as a linear cascade of airfoils. As we can see in figure 1.1, if we want to find the aerodynamic performance (specifically lift and drag) of an airfoil residing in a linear cascade, we need to take into account the surrounding airfoils, keeping in mind that the cascade extends to infinity in both directions. As the solidity increases, the airfoils in the cascade get closer together, and as the stagger angle of the blade section increases, the airfoils shift accordingly. Therefore we need some way to model the effects of changes in solidity and stagger on the linear cascade performance in addition to the nominal shape of the airfoil.

One such tool for viscous linear cascade analysis is MISES.¹ MISES couples an Euler method and viscous boundary layer model applied with periodic boundary conditions in order to model viscous linear cascade aerodynamics. Unfortunately, like many legacy codes, MISES is not particularly robust nor does it provide sufficiently smooth outputs in order to be used directly in optimization. Using MISES data, however, we can develop a surrogate of the data that is sufficiently smooth and robust for gradient-based optimization.

¹ Drela, *MISES*, 2009.

There are many methods for developing surrogate models, but we found a straightforward approach using a combination of splines to be most robust and accurate. We first use MISES to generate sets of lift and drag values given section thickness, solidity, stagger, and angle of attack. We then manually pre-process those lift and drag vs angle of attack polars to smooth them out and extend them as needed in order to have consistent angles for each combination of section geometries. We then take the lift and drag polars for sets of solidity and stagger at single thickness values and fit 3D B-Spline surfaces to those sets of polars. Finally, in the optimization we sample each B-Spline surface for thicknesses across the range of design variable bounds and then apply an Akima interpolation between the surfaces relative to selected thickness to determine the appropriate lift and drag polars for that iteration and the associated solidity, stagger, and blade thickness at each blade section.

1.2 Structural Model

Note that the majority of the text in this section was produced by Tyler Critchfield.

In order to model the structures of rotor blades, we approximate each rotor blade as a cantilever beam and apply geometrically exact beam theory (GEBT).^{2,3} GEBT accurately captures nonlinear effects of highly flexible and slender beams, including finite displacements, and coupled bending-torsion-shear behavior. In this work, we use GXBeam.jl,⁴ a Julia package that enables efficient computation of exact automatic derivatives through the entire structural model and has been applied successfully to the structural analysis of rotors in gradient-based optimization applications.^{5,6}

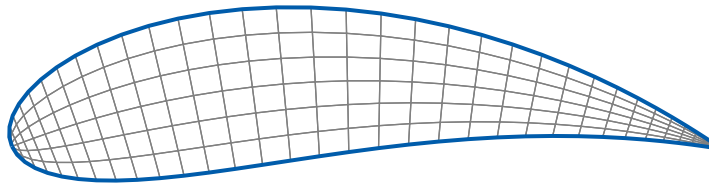


Figure 1.2: An example airfoil section showing the structural mesh (in gray) refined to the point of less than 1% change in section structural parameters. Specifically, 35 elements in the x-direction and 6 elements in the y-direction.

Perhaps the most vital inputs to GEBT methods are the stiffness and inertial properties of cross-sectional sections defined along the beam. We calculate these cross-sectional stiffness and inertial properties at each beam element's center using using a 2-D, finite element procedure⁷ that uses bi-linear quadrilateral elements in the mesh (see figure 1.2 for an example mesh). For each optimization iteration, we define the mesh nodes at the same relative positions on the airfoil. Mesh node locations are then adjusted based on changes to the airfoil thickness at each optimization iteration; and therefore changes in the mesh happen in a smooth manner.

For the optimizations in this work, we perform a set of steady-state structural analyses (one for each operating condition), where we fix the root section of the rotor blade in place and allow deflection along the rest of the blade. We use a beam reference frame that rotates around the rotor hub at a rate equal to that of the rotor rotation rate. We define the structural beam elements using the same set of radial locations we use to define the aerodynamic blade elements. Since the aerodynamic blade elements and structural beam elements are defined using the same set of coordinates, we apply aerodynamic forces and moments from the aerodynamic model for each blade element directly to the corresponding beam elements as linearly varying distributed loads. For all rotor blades, we assume a solid aluminum or polyoxymethylene (POM) with material properties tabulated in ?? where E is Young's modulus, G is the shear

2 Yu *et al.*, "GEBT: A general-purpose nonlinear analysis tool for composite beams," 2012.

3 Wang *et al.*, "Geometrically nonlinear analysis of composite beams using Wiener-Milenković parameters," 2017.

4 McDonnell *et al.*, "GXBeam: A Pure Julia Implementation of Geometrically Exact Beam Theory," 2022.

5 McDonnell *et al.*, "Geometrically Exact Beam Theory for Gradient-Based Optimization," 2024.

6 Critchfield *et al.*, "Mission-Focused Multidisciplinary Design Optimization of Tilt-Rotor eVTOL Propulsion System," 2025.

7 Giavotto *et al.*, "Anisotropic beam theory and applications," 1983.

modulus, ν is Poisson's ratio, ρ is material density, σ is the tensile and compressive strength, and τ is the shear strength.

Table 1.1: Aluminum and POM material properties used in this work.

	E (GPa)	G (GPa)	ν	ρ (kg/m ³)	σ_c (MPa)	σ_t (MPa)	τ (MPa)
Aluminum	70	26	0.3	2700	275	275	200
POM	3	3	0.44	1400	150	50	83

1.3 Acoustic Model

Note that the majority of this section was produced by Eduardo Alvarez.

In this work, we use an in-duct noise propagation code developed at Whisper Aero that is designed for application in gradient-based optimization. The code is based on the Goldstein acoustic analogy⁸, which is a generalization of the Ffowcs Williams–Hawkings analogy⁹ for an annular duct and center body. Note that for this work, we only model rotor tonal noise at the blade-passing frequency from thickness and loading aeroacoustic sources. Most of the implementation (summarized in the following subsections) follows the unified formulation for predicting steady and unsteady sources of rotor/stator noise by Moreau.¹⁰

⁸ Goldstein, *Aeroacoustics*, 1976.

⁹ , "Sound generation by turbulence and surfaces in arbitrary motion," 1969.

¹⁰ Moreau, "A unified analytical approach for the acoustic conceptual design of fans of modern aero-engines," 2016.

1.3.1 Modal Decomposition and Propagation

Given a cylindrical coordinate system, (z, r, θ) , with temporal variable, t , an acoustic pressure wave p can be represented by its Fourier transform as

$$p(z, r, \theta, t) = \sum_{\omega} p^{\omega}(z, r, \theta) e^{i\omega t}, \quad (1.1)$$

where $p^{\omega}(z, r, \theta)$ is the spectral pressure, or coefficient of the Fourier transform for frequency ω . The spectral pressure can then be decomposed into circumferential modes, m , as

$$p^{\omega}(z, r, \theta) = \sum_{m=-\infty}^{+\infty} p_m^{\omega}(z, r) e^{im\theta}. \quad (1.2)$$

The modal pressure, p_m^{ω} are then in turn decomposed into radial modes, n , as

$$p_m^{\omega}(z, r) = \sum_{n=0}^{+\infty} A_{mn}^{\pm} \frac{J_m(\kappa_{mn}^v \frac{r}{R_{\text{duct}}}) + Q_{mn} Y_m(\kappa_{mn}^v \frac{r}{R_{\text{duct}}})}{\sqrt{F_{mn}}} e^{ik_z^{\pm} z} \quad (1.3)$$

where J_m and Y_m are the Bessel functions of the first and second kind of order m , respectively; k_z^{\pm} is the axial wave number (note the \pm superscript

indicates direction of propagation with + being downstream); ν is the hub-to-duct ratio $\nu \equiv \frac{R_{\text{hub}}}{R_{\text{duct}}}$; and κ_{mn}^ν and Q_{mn}^ν are the eigenvalue and coefficient, respectively, of the boundary-condition equation for concentric cylindrical walls:

$$\begin{aligned} J'_m(k) + QY'_m(k) &= 0, \\ J'_m(\nu k) + QY'_m(\nu k) &= 0; \end{aligned} \quad (1.4)$$

and F_{mn} is a normalization factor:

$$F_{mn} = \frac{1 - \nu^2}{2}. \quad (1.5)$$

Thus, the modal amplitudes A_{mn}^\pm are the only unknowns required to define the acoustic pressure wave $p(z, r, \theta, t)$ of equation (1.1), and these modal amplitudes fully characterize the pressure wave everywhere along the duct over time.

Notice in equation (1.3) that the basis $e^{ik_z^\pm z}$ indicates that any mode associated with an imaginary wave number k_z^\pm will decay exponentially fast along the length of the duct, thus hinting at the existence of cut-off modes that might not propagate out of the duct provided that the duct is sufficiently long. This is consistent with the cut-off theory of Tyler and Sofrin.¹¹

11 Tyler *et al.*, "Axial Flow Compressor Noise Studies," 1962.

1.3.2 Acoustic Analogy

In order to compute the unknown modal amplitudes, we start with Goldstein's generalization of the Ffowcs Williams–Hawkings equation⁹ which is in turn a generalization of Lighthill's acoustic analogy¹² which describes the acoustic pressure caused by acoustic sources in relative motion with respect to a hard surface.

9 , "Sound generation by turbulence and surfaces in arbitrary motion," 1969.

12 , "On sound generated aerodynamically I. General theory," 1952.

$$p(X, t) = \frac{1}{t_{\text{ref}}} \int_{-\infty}^{+\infty} \left[- \int \int \left(\underbrace{\rho_0 W_n \frac{DG}{Dt_s}}_{\text{thickness}} + \underbrace{f_i \frac{\partial G}{\partial X_{s_i}}}_{\text{loading}} \right) dX_s + \int \int \int \underbrace{T_{ij} \frac{\partial^2 G}{\partial X_{s_i} \partial X_{s_j}}}_{\text{turbulence}} dX_s \right] dt_s, \quad (1.6)$$

where t_{ref} is the reference time scale, ρ_0 is the air density, W_n is the normal velocity, f_i is the loading force, X is the position in three-dimensional space, the subscript (s) indicates values of the acoustic source, T_{ij} is the Lighthill tensor, and G is the Green's function associated to the Laplace equation posed by the Lighthill acoustic analogy. In this work, we focus on the thickness and loading terms of equation (1.6), neglecting the quadrupole turbulent term (as is common).

As opposed to the open-rotor case, where G is the free-field Green's function, G for in-duct acoustics is a more complicated compilation of Bessel functions that impose the boundary condition of zero pressure gradient along a concentric cylindrical duct. Specifically, in the in-duct

case G is obtained by decomposing the Green's function in Fourier series in the frequency domain as well as into circumferential modes,

$$G(X, t, X_s, t_s) = \frac{t_{\text{ref}}}{2\pi} \int_{-\infty}^{+\infty} \sum_{m=-\infty}^{+\infty} G_m^\omega(z, r, z_s, r_s) e^{im(\theta-\theta_s)-i\omega(t-t_s)} d\omega \quad (1.7)$$

$$G_m^\omega(z, r, z_s, r_s) = g_m^\omega(z, r, r_s) e^{-ik_z z_s} \quad (1.8)$$

where the kernel g_m^ω is calculated as

$$g_m^\omega(z, r, r_s) = \sum_{n=0}^{\infty} \frac{E_{mn}^\nu(r/R_{\text{duct}})}{\sqrt{F_{mn}}} e^{ik_z^\pm z} \hat{g}_{mn}^\omega(r_s), \quad (1.9)$$

where

$$\hat{g}_{mn}^\omega(r_s) = \frac{i}{4\pi R_{\text{duct}}} \frac{E_{mn}^\nu(r_s/R_{\text{duct}})}{k R_{\text{duct}} \alpha_{mn} \sqrt{F_{mn}}}, \quad (1.10)$$

$$E_{mn}^\nu(\varrho) = J_m(k_{mn}^\nu \varrho) + Q_{mn}^\nu Y_m(k_{mn}^\nu \varrho), \quad (1.11)$$

and α_{mn} is the mode cut-on factor defined as:

$$\alpha_{mn} = \left[1 - (1 - M_x^2) \left(\frac{\kappa_{mn}^\nu}{k R_{\text{duct}}} \right)^2 \right]^{1/2}. \quad (1.12)$$

which for propagating modes is a real number between 0 and 1, and for non-propagation modes (referred to as cut-off modes), α_{mn} is purely imaginary.

Using, equation (1.10), equation (1.3), and an expression for modal pressure for a rotating rotor, Moreau develops the following expression for the unknown modal amplitudes of equation (1.3) associated with thickness, lift force, and quadrupole sources which integrated across the rotor blade span (from R_{hub} to R_{tip}) and summed over the number of blades, N_B :

$$A_{mn}^\pm = -i \sum_{b=1}^{N_B} \int_{R_{\text{hub}}}^{R_{\text{tip}}} \hat{g}_{mn}^\omega \cdot e^{-ik_z z_{LE} - im\Lambda_{LE}} \cdot \sigma dr_s, \quad (1.13)$$

where σ is the source strength of an arbitrary tonal noise component detailed in the next section.

1.3.3 Tonal Noise Sources

To obtain the values for σ , we employ the unifying formulation of Moreau in which all tonal sources (steady and unsteady) are expressed as

$$\sigma(r_s, \omega, \tilde{\omega}) = \underbrace{\mathcal{R}(r_s, \omega)}_{\text{acoustic radiation}} \cdot \underbrace{\Psi(r_s, \omega)}_{\text{chord-wise correlation}} \cdot \underbrace{\chi_0(r_s, \tilde{\omega})}_{\text{aerodynamic excitation}} \cdot \underbrace{e^{i\phi_0(r_s, \tilde{\omega})}}_{\text{phase of excitation}}; \quad (1.14)$$

where in this work we model only rotor tonal noise at the blade-passing frequency from steady thickness and lift loading sources—with specific terms calculated as shown in Table 1.2.

Table 1.2: Tonal noise sources included in this study.

Source	\mathcal{R}	Ψ	χ_0	ϕ_0
Thickness Terms	$k_\ell^2 c^2$	$\frac{1}{c} \int_{\ell=0}^c h_T(\ell) e^{-ik_\ell \ell} d\ell$	$\rho_0 W_0^2 \frac{\bar{t}}{c}$	0
Lift Loading Terms	$ik_n c$	$\frac{1}{c} \int_{\ell=0}^c h_L(\ell) e^{-ik_\ell \ell} d\ell$	$\frac{1}{2} \rho_0 W_0^2 C_L$	0

where k_ℓ and k_n are the chord-wise and blade normal wave numbers, respectively; h_T and h_L are the thickness and loading distributions, respectively; c , \bar{t}/c , ρ_0 , W_0 , and C_L are the chord length, thickness to chord ratio, local density, local inflow velocity, and lift coefficient of the blade section, respectively.

Additional details of the implementation developed by Eduardo Alvarez are contained in an article in preparation at the time of producing this dissertation.¹³ Those additional details include an efficient method for pre-decomposition of the chord-wise distributions to allow for fast evaluation of the integrals for the Ψ terms, as well as a gradient-based optimization friendly method for modeling finite-duct cut-off modes. Note that the finite-duct model is somewhat ad-hoc, and while capturing trends sufficient for optimization purposes, is perhaps not useful for accurate analysis.

¹³ Mehr *et al.*, “Aero-Structural-Acoustic Gradient-based Optimization of Electric Ducted Fans,” 2025.

Chapter 1 References

- 1 Drela, M., *MISES*, version 2.64, December 14, 2009. URL: <https://web.mit.edu/drela/Public/web/mises/>. cited on p. 2
- 2 Yu, W. and Blair, M., “GEBT: A general-purpose nonlinear analysis tool for composite beams,” *Composite Structures*, vol. 94, no. 9, 2012, pp. 2677–2689. DOI: 10.1016/j.compstruct.2012.04.007 cited on p. 3
- 3 Wang, Q. and Yu, W., “Geometrically nonlinear analysis of composite beams using Wiener-Milenković parameters,” *Journal of Renewable and Sustainable Energy*, vol. 9, no. 3, June 2017, p. 033 306. DOI: 10.1063/1.498 5091 cited on p. 3
- 4 McDonnell, T. and Ning, A., “GXBeam: A Pure Julia Implementation of Geometrically Exact Beam Theory,” *Journal of Open Source Software*, vol. 7, no. 73, May 2022, p. 3997. DOI: 10.21105/joss.03997 cited on p. 3
- 5 McDonnell, T. and Ning, A., “Geometrically Exact Beam Theory for Gradient-Based Optimization,” *Computers & Structures*, vol. 298, no. 107373, July 2024. DOI: 10.1016/j.compstruc.2024.107373 cited on p. 3
cited on p. 3

- 6 Critchfield, T. and Ning, A., “Mission-Focused Multidisciplinary Design Optimization of Tilt-Rotor eVTOL Propulsion System,” *Journal of Aircraft* (In Review), 2025.
- 7 Giavotto, V., Borri, M., Mantegazza, P., Ghiringhelli, G., Carmaschi, V., Maffioli, G., and Mussi, F., “Anisotropic beam theory and applications,” *Computers & Structures*, vol. 16, no. 1-4, 1983, pp. 403–413. DOI: 10.1016/0045-7949(83)90179-7 cited on p. 3
- 8 Goldstein, M., *Aeroacoustics*, ser. Advanced book program. McGraw-Hill International Book Company, 1976. cited on p. 4
- 9 , “Sound generation by turbulence and surfaces in arbitrary motion,” en, *Philosophical Transactions of the Royal Society of London. Series A, Mathematical and Physical Sciences*, vol. 264, no. 1151, May 1969, pp. 321–342. DOI: 10.1098/rsta.1969.0031 cited on pp. 4, 5
- 10 Moreau, A., “A unified analytical approach for the acoustic conceptual design of fans of modern aero-engines,” Ph.D. Dissertation, Technische Universität Berlin, July 2016. cited on pp. 4, 6
- 11 Tyler, J. M. and Sofrin, T. G., “Axial Flow Compressor Noise Studies,” January 1962, p. 620 532. DOI: 10.4271/620532 cited on p. 5
- 12 , “On sound generated aerodynamically I. General theory,” en, *Proceedings of the Royal Society of London. Series A. Mathematical and Physical Sciences*, vol. 211, no. 1107, March 1952, pp. 564–587. DOI: 10.1098/rspa.1952.0060 cited on p. 5
- 13 Mehr, J., Critchfield, T., Ning, A., and Alvarez, E., “Aero-Structural-Acoustic Gradient-based Optimization of Electric Ducted Fans,” *Manuscript in preparation*, 2025. cited on p. 7

Great things are done by a series of small things brought together.

— Vincent Van Gogh

There are many new and exciting technologies employing distributed electric propulsion, including applications for advanced air mobility (AAM). The novelty of new technologies and applications, however, inevitably leads to novel problems that must be solved before widespread acceptance is achieved. Of note for many AAM applications is the trade between aerodynamic performance and noise generation. Electric ducted fans (EDF) have been suggested as potentially able to meet both performance and noise generation constraints, but there is still work to be done to determine the extent of EDF capabilities. In this chapter, we utilize gradient-based optimization, in conjunction with low-cost analysis tools, to explore the aero-structural-acoustic design space for EDF in the context of AAM. By employing low-cost analysis tools in a gradient-based optimization setting, we are able to optimize a larger-than-average number of design variables—across aerodynamic, structural, and acoustic disciplines. Our object for this chapter is to determine trends in aero-structural-acoustic trades that will be helpful to focus further, higher fidelity, analysis of EDF technologies.

2.1 Optimization Methods

For the optimizations in this work, we select an expended energy minimization problem:

Minimize energy expenditure;
with respect to: duct geometry, rotor geometry, rotor rotation rate;
subject to: required thrusts, maximum sound level, maximum structural deflection.

(2.1)

We compare across two application cases: a 20 lb. eVTOL UAS, and a 55 lb. eCTOL UAS. The major aircraft parameters used to define the objective and thrust constraints are shown in Table 2.1.

To estimate the energy expenditure, we take the rotor power from each operating point (static, climb, cruise) and multiply them by the respective times in each condition and then sum the resulting energies. We make some assumptions here, namely that the static thrust is constant

Table 2.1: Major vehicle parameters used for the optimizations in this chapter.

Parameter	eVTOL	eCTOL
Number of Propulsors (N_p)	2	1
Nominal Takeoff Weight lbs.	20	55
Static Thrust to MTOW ($\frac{T}{W}$) _s	1.0	0.35
Cruise Velocity (V_{cr}) mph	45	50
Climb Velocity (V_{cl}) mph	25	30
Cruise Lift/Drag ($\frac{L}{D}$) _{cr}	12	12
Climb Lift/Drag ($\frac{L}{D}$) _{cl}	10	10
Cruise Altitude (A_{cr}) ft	400	1500
Climb Angle (γ_{cl}) degrees	10	5
Cruise Range (R_{cr}) mi	20	30

during takeoff, climb happens at a constant velocity, and we neglect energy expense during approach for both cases as well as landing for the CTOL case. Therefore the time in static thrust for the VTOL case is divided between takeoff and landing and the time in static thrust for the CTOL case is just takeoff. When calculating the power for climb, we also take a single operating point at an altitude half-way between sea level and the cruise altitude. We additionally assume the static condition takes place at sea level. Together we have

$$E_{tot} = P_s t_s + P_{cl} t_{cl} + P_{cr} t_{cr} \quad (2.2)$$

The various times (in seconds) for each operating condition are give by

$$\begin{aligned} t_s &= 10 \\ t_{cl} &= \frac{A_{cr}}{V_{cl} \sin(\gamma_{cl})}, \\ t_{cr} &= \frac{R_{cr}}{V_{cr}}. \end{aligned} \quad (2.3)$$

The thrust constraints for static, climb, and cruise conditions are defined based on the maximum takeoff weight, MTOW, to be

$$\text{Static Thrust} = \frac{\text{MTOW} \frac{T_s}{W}}{N_p}; \quad (2.4a)$$

$$\text{Climb Thrust} = \frac{\text{MTOW}}{N_p} \left[\frac{1}{(\frac{L}{D})_{cl}} + \sin(\gamma_{cl}) \right]; \quad (2.4b)$$

$$\text{Cruise Thrust} = \frac{\text{MTOW}}{(\frac{L}{D})_{cr} N_p}; \quad (2.4c)$$

Note in Table 2.1 that we set the nominal takeoff weight of the aircraft. For the thrust constraints, we add to that nominal weight the weight of the duct shroud and center body and the blade weight. The total weights of the duct bodies and rotor blades are not particularly large relative to the nominal vehicle weight, but as we will be changing duct and rotor geometries in these studies, the thrust requirements should be updated accordingly. We assume the motor weight stays constant and is included in the nominal vehicle weight. To determine the rotor weight, we simply take the mass of the blade as determined by the structural model, multiply by the number of blades, and multiply by gravity to obtain a weight. For the duct shroud and center body, we assume a 2mm thick carbon fiber reinforced polymer shell structure and compute the surface area of the bodies, multiply by the thickness and density to get the mass, and the multiply by gravity to get a weight.

For the rotor structural constraints, we constrain the rotor blade tip to deflect no more than 1% of the blade radius and rotate no more than 1 degree. Using the Tsai-Wu failure criteria,¹⁴ we found that for both materials used in this study, our deflection and rotation constraints were violated far before material failure was reached. Therefore we only use the deflection and rotation constraints and do not apply any material failure constraints as they would be inactive.

¹⁴ Tsai *et al.*, "A General Theory of Strength for Anisotropic Materials," 1971.

2.1.1 Geometry and Geometric Design Variables

For the overall configuration, we start with rotor diameters of about 4 in. for the eVTOL case and roughly 6 in. for the eCTOL case. We vary the duct chord length between 1 and 2 times the rotor radius in the following studies. We place the rotor at the midpoint of the duct to allow a reasonable inlet length. We set the center body to begin aft of the duct leading edge, and keep its position relative to the duct leading edge constant for simplicity. We extend the center body slightly aft of the duct trailing edge and also keep its position relative to the duct trailing edge constant to avoid discontinuities in relative panel position. We maintain a constant rotor hub to tip ratio of 0.25 as a constant hub to tip ratio allows significant levels of precomputation for our acoustics models, making the optimization process more efficient. Figure 2.1 shows a meridional view of an example duct and center body geometries with rotor lifting line location.

Rotor geometry design variables include chord and twist values along the blade as well as blade element thickness. To encourage manufacturable designs, we use four design variables spaced equally along the blade for chord, twist, and blade element thickness. We also apply several linear constraints to the chord, twist, and thickness variables to avoid many changes in concavity that could make manufacture difficult or infeasible. We pre-select 11 positions along the blade for analysis and linearly interpolate between the design variables to obtain the values for analysis. An example of the chord and twist interpolation is shown in figure 2.2.

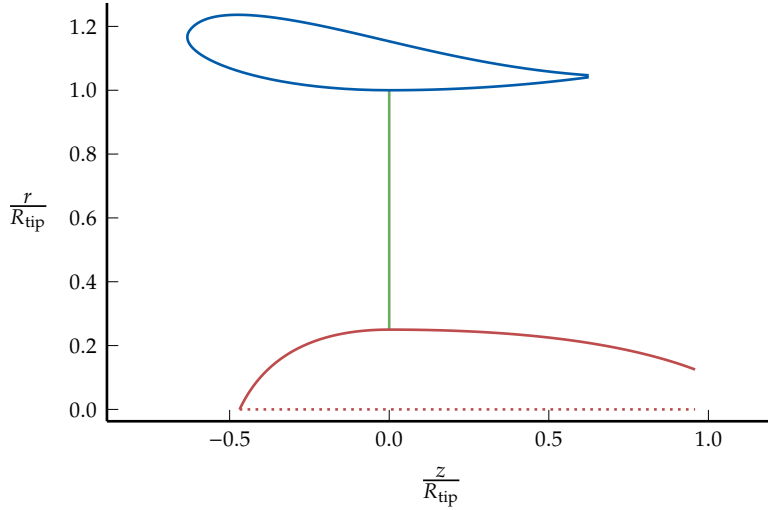
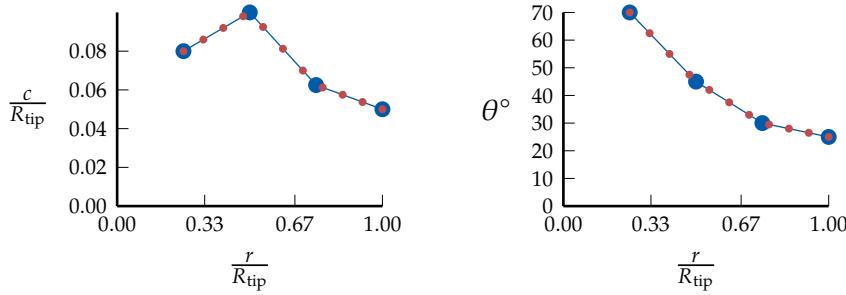


Figure 2.1: Meridional view of example geometry.



(a) Example chord (c) parameterization. **(b)** Example twist (θ) parameterization.

Figure 2.2: Visual explanation of the rotor geometry parameterization employed in this chapter. **Blue circles** indicate design variables, and **smaller red circles** indicate interpolated points for analysis.

We generate the specific duct and center body geometries with a composition of B-Spline curves. For the duct casing, we first define two quadratic B-Splines that meet at the center of the duct (where the rotor is placed). The first of these quadratic B-Splines is the green spline with square control points shown in figure 2.3, and the second is the red spline with diamond control points. The radial position of the first control point of the spline which is situated ahead of the rotor (the green one with square control points) is a design variable that controls inlet area (see the tick labeled I_1 , in figure 2.3). Similarly, the radial position of the last control point of the spline which is situated behind the rotor (the red one with diamond control points) is a design variable that controls the exit area (see tick labeled O_3 , in figure 2.3). To define the specific casing geometry, we want a round leading edge and a sharp trailing edge. To get a round leading edge, we define an additional cubic B-Spline (see the other red spline with circle control points in figure 2.3) that

has three of the same control points as the front quadratic B-Spline (see the overlapping green square and red circle control points in figure 2.3). The cubic spline includes one additional control point (the red circle out in front in figure 2.3) placed along the normal vector (represented by a dotted line) relative to the end of the quadratic spline. Using a cubic spline here gives us a round leading edge, rather than the corner seen between the green and blue lines in figure 2.3. Placing the point along the normal vector results in the casing and nacelle surfaces to be tangent at the leading edge. The distance of the control point along the normal controls the leading edge radius of the casing and is fixed for the optimizations in this work. The quadratic spline aft of the rotor (red with diamond control points) already results in a sharp trailing edge, so we use that for the back half of the casing geometry. We set the remaining control points of all of the B-Splines in such a way that the casing surfaces ahead of and behind the rotor smoothly connect at their junction (note all of the points along the dotted line at $r = R_{\text{tip}}$ in figure 2.3). To define the duct nacelle geometry, we use another cubic B-Spline (in blue in figure 2.3). We place the first and second control points at the leading edge similar how the casing spline points are positioned to ensure tangency at the leading edge. We also place two additional control points whose radial positions (N_{3r} and N_{4r}) are design variables that control the remaining details of the nacelle surface. An example of the duct geometry is shown in figure 2.3 where the blue line and triangle markers are the nacelle surface and control points, the red line with circle control points is the casing geometry ahead of the rotor, the red line with diamond control points is the casing geometry aft of the rotor, and the green line with square control points is the quadratic B-Spline to which the casing and nacelle geometries are relative ahead of the rotor.

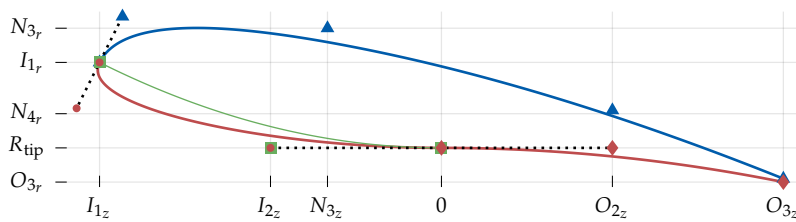


Figure 2.3: Visual explanation of the duct geometry parameterization employed in this chapter. **Nacelle** and **casing** curves as well as **front quadratic B-Spline**. Black dotted lines indicate control points placed to enforce continuity.

As noted in ??, it is helpful to apply some additional constraints to the duct geometry parameters to ensure a robust and feasible solution—avoiding difficult to model, viscous dominant, highly separated flow conditions. Specifically, we keep the leading edge radius constant, apply a maximum inlet radius constraint, and constrain the cross-sectional thickness to be at least 14% of the duct chord. In addition, we apply a constraint to the penultimate nacelle control point that ensure a reasonable

trailing edge wedge angle.

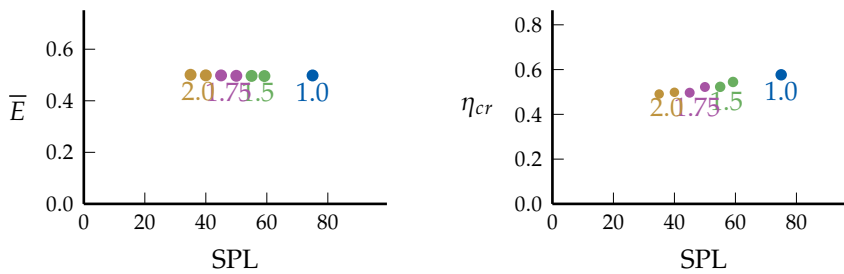
2.1.2 Optimizer and Solver Settings

For the optimizations in this work, we use Sparse Nonlinear OPTimizer (SNOPT), a sequential quadratic programming algorithm for large-scale, constrained optimization [15]. For the most part we keep the various settings in SNOPT as their default values. To provide SNOPT with a Jacobian of the objective and constraint functions, we use ForwardDiff.jl, a Julia package for forward mode automatic differentiation [16].

2.2 Optimization Studies

Show effects of sweeping duct length in VTOL case

figure showing energy vs spl for various duct lengths discuss trends seen as well as takeaways. keeping practical considerations in mind (e.g. non-axisymmetric conditions require longer inlets for better performance), discuss trades and takeaways in longer vs shorter ducts.



(a) Optimal relative energy expenditure vs (b) Cruise efficiency vs sound power level

Figure 2.4: VTOL case energy and efficiency vs sound power level across a series of duct lengths at a blade count of 7 with aluminum blades.

Figure 2.4(a) shows the relative energy vs sound power level at various duct lengths for the VTOL case with aluminum blades at a blade count of 7. As expected, longer ducts cut-off more acoustic modes than shorter duct lengths, leading to decreased sound power levels at the duct inlet and exit as the duct length increases. In addition, we see bands of sound power levels for each duct length indicating that on one hand, a specific duct length will nominally have a maximum sound power level for a given set of thrust constraints, and on the other hand, there is a limit to the physical feasibility of how quiet a specific figuration can be before aerodynamic or structural limits are reached. **TODO: probably want to discuss which limits are reached in this case. If thrust can change a bit, it must be an inactive constraint somewhere.** Interestingly, we are able to keep a nearly constant optimal energy (though there is a minimal general increase in energy expenditure as the duct length increases). Figure 2.4(b) shows the total cruise efficiency (η_{cr}) vs sound power level, and, by virtue of the change in efficiency, indicates that although the optimal energy stays nearly the same, the thrust must change more significantly with

changes in duct length. **TODO: look at thrust and see which, if any cases the thrust constraint is active. are there some cases where it's not active?**

discuss change (or lack thereof) in energy across duct lengths and set up discussion of what might cause that. TO check: - inviscid vs viscous body thrust components - why is energy basically the same even with a 5dB change and then impossible constraints after that? How does the energy come out so similar? figure showing change in thrust figure showing change in efficiency with duct length discussion about trade in efficiency and whether that's important if the energy comes out the same?

figure comparing rotor solidity, twist, thickness, and RPM at ends and maybe a middle spot of the duct length sweep. discuss how the differences in rotor geometry and rpm lead to the energies and SPLs seen in the figures above. **TODO: CONSIDER LOOKING AT ROTOR GEOMETRY FOR ONE DUCT LENGTH AT SEVERAL ACOUSTICS, AND MAYBE COMPARE TO ANOTHER CASE AS WELL SOMEHOW TO SHOW HOW THE TRENDS ARE THE SAME, BUT THE DUCT LENGTH SHIFTS acoustics OVER.** Will want to do this for two cases that are unconstrained, and then will want to specifically run optimizations at acoustic constraints the exact same distance from the unconstrained values. e.g. unconstrained spls are 73.5 and 52.7, then we need to run at those -5dB or something in order to compare properly

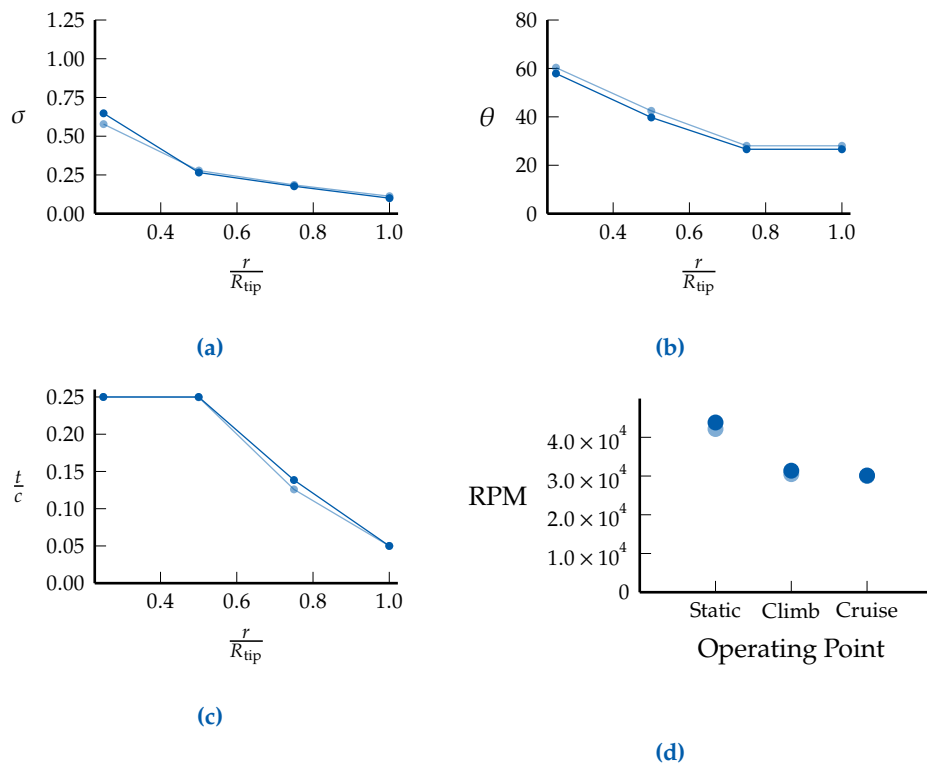


Figure 2.5: duct length sweep rotor comparison at a single spl or some relevant and helpful comparison cases

If it is helpful, show the duct and blade weight in ounces if it adds to the discussion here. If not, save the mass stuff for the Al/POM comparison later.

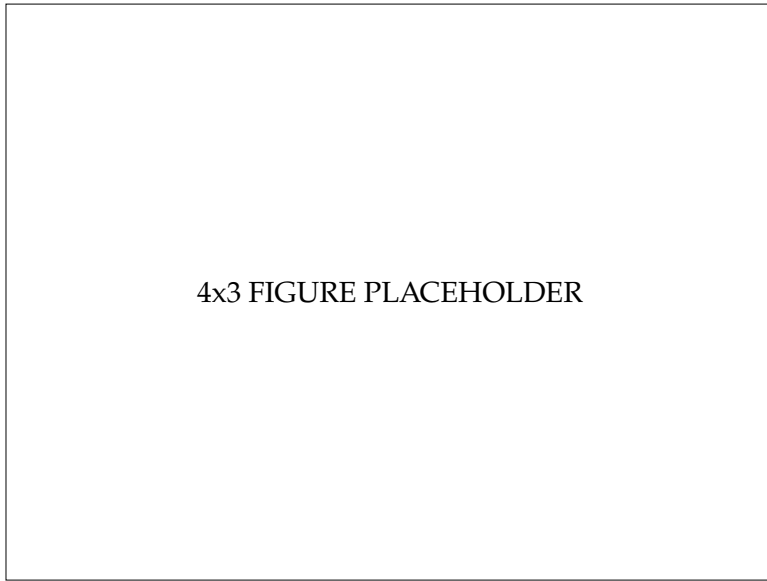
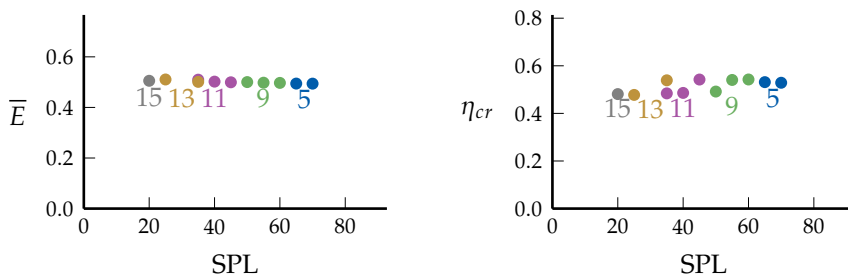


Figure 2.6: duct + rotor weight in oz.

REPEAT everything for the number of blade sweep.

figure showing energy vs spl for various blade counts discuss trends seen as well as takeaways. keeping practical considerations in mind (e.g. non-axisymmetric conditions require longer inlets for better performance), discuss trades and takeaways in longer vs shorter ducts.



(a) Optimal relative energy expenditure vs (b) Cruise efficiency vs sound power level

Figure 2.7: VTOL case energy and efficiency vs sound power level across various numbers of aluminum blades at a duct length of $1.5R_{tip}$.

Figure 2.7(a) shows the relative energy expenditure of the VTOL case for aluminum blades and a duct length of $1.5R_{tip}$ across a range of blade counts. We immediately see that for the most part, the energy expenditure is quite similar across the range of blade counts. Interestingly, before we see appreciable increases in energy, we actually run into infeasibilities in the trade between thrust and acoustics. Specifically, as the acoustic

constraint is cranked down more than 10 dB or so, the design cannot meet both the acoustic and thrust constraint simultaneously. On the other end of the spectrum, at increasing blade counts the optimal design results in an already quieter design than smaller blade counts. Despite there being some overlap, there are clear bands of sound power levels for each blade count.

figure showing energy vs duct length at a constant acoustic value if possible (focus in on one acoustic level with overlap, may want to show 2 spots if there isn't a lot of overlap. or maybe show the closest you can get with the other cases.) discuss change (or lack thereof) in energy across duct lengths and set up discussion of what might cause that.

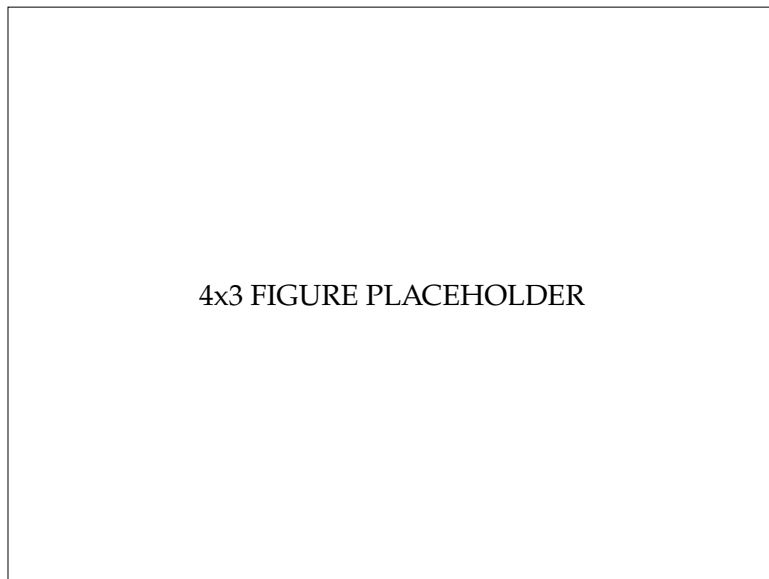


Figure 2.8: energy vs blade count for a single acoustic constraint.

figure comparing rotor solidity, twist, thickness, and RPM at ends and maybe a middle spot of the blade count sweep. discuss how the differences in rotor geometry and rpm lead to the energies and SPLs seen in the figures above.

If it is helpful, show the duct and blade weight in ounces if it adds to the discussion here. If not, save the mass stuff for the Al/POM comparison later.

If energies are basically the same across the board, then want to add some discussion on why they are the same as well as show why simply matching the solidities and RPMs doesn't automatically work (for example higher solidity at lower blade count should increase SPL I think). Perhaps add a figure for a case where you set the solidities, twists, thickness, and RPM the same for different blade counts or something and report the acoustics. idk.

REPEAT VTOL Stuff for CTOL case, but if trends are identical, maybe abbreviate and not include all the same plots.

Show effects of sweeping duct length in CTOL case

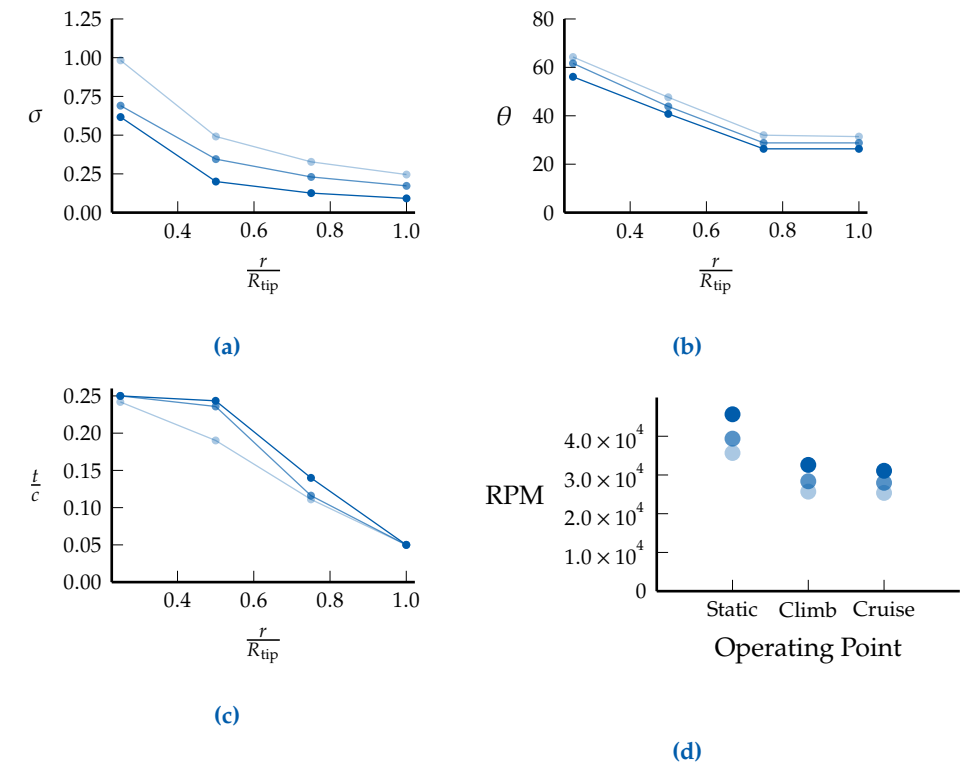


Figure 2.9: Rotor blade geometries for 5, 9, and 13 blades at 65, 60, and 20 dB, respectively

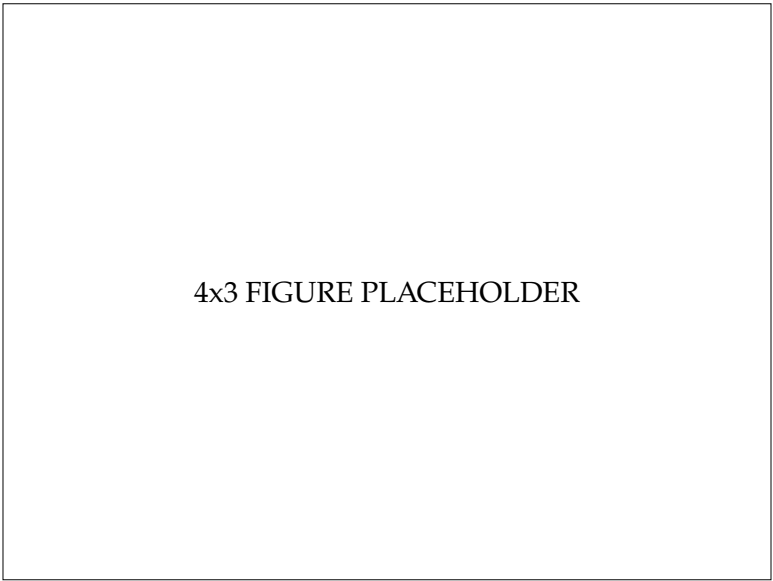
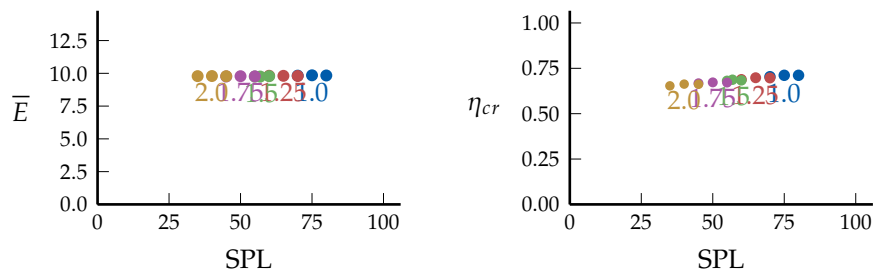


Figure 2.10: duct + rotor weight in oz.

figure showing energy vs spl for various duct lengths discuss trends seen as well as takeaways. keeping practical considerations in mind (e.g. non-axisymmetric conditions require longer inlets for better performance), discuss trades and takeaways in longer vs shorter ducts.

figure showing energy vs spl for various blade counts discuss trends

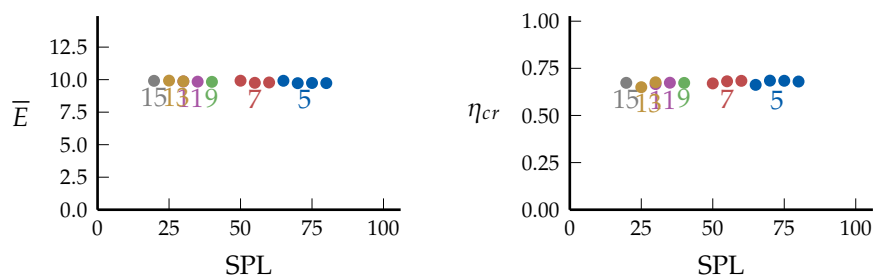


(a) Optimal relative energy expenditure vs sound power level

(b) Cruise efficiency vs sound power level

Figure 2.11: CTOL case energy and efficiency vs sound power level across a series of duct lengths at a blade count of 7 with aluminum blades.

seen as well as takeaways. keeping practical considerations in mind (e.g. non-axisymmetric conditions require longer inlets for better performance), discuss trades and takeaways in longer vs shorter ducts.



(a) Optimal relative energy expenditure vs sound power level

(b) Cruise efficiency vs sound power level

Figure 2.12: CTOL case energy and efficiency vs sound power level across various numbers of aluminum blades at a duct length of $1.5R_{tip}$.

Run POM optimizations once AI ones are done and see what might be interesting to plot and discuss. (mass probably, structures vs acoustics for not as constrained cases where POM is forced to be quieter, but that's due to structures maybe?)

Chapter 2 References

- 14 Tsai, S. W. and Wu, E. M., "A General Theory of Strength for Anisotropic Materials," *Journal of Composite Materials*, vol. 5, no. 1, 1971, pp. 58–80. cited on p. 11
DOI: <https://doi.org/10.1177/002199837100500106>
- 15 Gill, P. E., Murray, W., and Saunders, M. A., "SNOPT: An SQP Algorithm for Large-Scale Constrained Optimization," *SIAM Journal on Optimization*, vol. 12, no. 4, 2002, pp. 979–1006. DOI: 10.1137/s1052623499350013 cited on p. 14
- 16 Revels, J., Lubin, M., and Papamarkou, T., "Forward-Mode Automatic Differentiation in Julia," *ArXiv:1607.07892 [cs.MS]*, 2016. cited on p. 14

References

- 1 Drela, M., *MISES*, version 2.64, December 14, 2009. URL: <https://web.mit.edu/drela/Public/web/mises/>. cited on p. 2
- 2 Yu, W. and Blair, M., “GEBT: A general-purpose nonlinear analysis tool for composite beams,” *Composite Structures*, vol. 94, no. 9, 2012, pp. 2677–2689. DOI: 10.1016/j.compstruct.2012.04.007 cited on p. 3
- 3 Wang, Q. and Yu, W., “Geometrically nonlinear analysis of composite beams using Wiener-Milenković parameters,” *Journal of Renewable and Sustainable Energy*, vol. 9, no. 3, June 2017, p. 033 306. DOI: 10.1063/1.4985091 cited on p. 3
- 4 McDonnell, T. and Ning, A., “GXBeam: A Pure Julia Implementation of Geometrically Exact Beam Theory,” *Journal of Open Source Software*, vol. 7, no. 73, May 2022, p. 3997. DOI: 10.21105/joss.03997 cited on p. 3
- 5 McDonnell, T. and Ning, A., “Geometrically Exact Beam Theory for Gradient-Based Optimization,” *Computers & Structures*, vol. 298, no. 107373, July 2024. DOI: 10.1016/j.compstruc.2024.107373 cited on p. 3
- 6 Critchfield, T. and Ning, A., “Mission-Focused Multidisciplinary Design Optimization of Tilt-Rotor eVTOL Propulsion System,” *Journal of Aircraft* (In Review), 2025. cited on p. 3
- 7 Giavotto, V., Borri, M., Mantegazza, P., Ghiringhelli, G., Carmaschi, V., Maffioli, G., and Mussi, F., “Anisotropic beam theory and applications,” *Computers & Structures*, vol. 16, no. 1-4, 1983, pp. 403–413. DOI: 10.1016/0045-7949(83)90179-7 cited on p. 3
- 8 Goldstein, M., *Aeroacoustics*, ser. Advanced book program. McGraw-Hill International Book Company, 1976. cited on p. 4
- 9 , “Sound generation by turbulence and surfaces in arbitrary motion,” en, *Philosophical Transactions of the Royal Society of London. Series A, Mathematical and Physical Sciences*, vol. 264, no. 1151, May 1969, pp. 321–342. DOI: 10.1098/rsta.1969.0031 cited on pp. 4, 5
- 10 Moreau, A., “A unified analytical approach for the acoustic conceptual design of fans of modern aero-engines,” Ph.D. Dissertation, Technische Universität Berlin, July 2016. cited on pp. 4, 6
- 11 Tyler, J. M. and Sofrin, T. G., “Axial Flow Compressor Noise Studies,” January 1962, p. 620 532. DOI: 10.4271/620532 cited on p. 5

cited on p. 5

- 12 , “On sound generated aerodynamically I. General theory,” en, *Proceedings of the Royal Society of London. Series A. Mathematical and Physical Sciences*, vol. 211, no. 1107, March 1952, pp. 564–587. DOI: 10.1098/rspa.1952.0060
- 13 Mehr, J., Critchfield, T., Ning, A., and Alvarez, E., “Aero-Structural-Acoustic Gradient-based Optimization of Electric Ducted Fans,” *Manuscript in preparation*, 2025. cited on p. 7
- 14 Tsai, S. W. and Wu, E. M., “A General Theory of Strength for Anisotropic Materials,” *Journal of Composite Materials*, vol. 5, no. 1, 1971, pp. 58–80. DOI: <https://doi.org/10.1177/002199837100500106> cited on p. 11
- 15 Gill, P. E., Murray, W., and Saunders, M. A., “SNOPT: An SQP Algorithm for Large-Scale Constrained Optimization,” *SIAM Journal on Optimization*, vol. 12, no. 4, 2002, pp. 979–1006. DOI: 10.1137/s1052623499350013 cited on p. 14
- 16 Revels, J., Lubin, M., and Papamarkou, T., “Forward-Mode Automatic Differentiation in Julia,” *ArXiv:1607.07892 [cs.MS]*, 2016. cited on p. 14